

Benchmark of density functional theory for superconductors in elemental materials

Mitsuaki Kawamura,^{1,*} Yuma Hizume,² and Taisuke Ozaki¹

¹*Institute for Solid State Physics, The University of Tokyo, Kashiwa 277-8581, Japan*

²*Department of Physics, The University of Tokyo, Tokyo 113-0033, Japan*

(Dated: December 21, 2024)

Systematic benchmark calculations for elemental bulks are presented to validate the accuracy of density functional theory for superconductors. We develop a method to treat the spin-orbit interaction (SOI) together with the spin fluctuation (SF) and examine their effect on the superconducting transition temperature. From the benchmark calculations, we find the following results: (1) The calculations, including SOI and SF, reproduce the experimental superconducting transition temperature (T_c) quantitatively. (2) The effect by SOI is small excepting a few elements such as Pb, Tl, and Re. (3) SF reduces T_c s, especially for the transition metals, while this reduction is too weak to reproduce the T_c s of Zn and Cd. (4) We reproduce the absence of superconductivity for alkaline (earth) and noble metals. These calculations confirm that this method is applicable to the wide range of materials and imply a direction for the further improvement of the methodology.

I. INTRODUCTION

The first-principles calculation of the superconducting properties such as the transition temperature (T_c) and the gap function is of great interest to explore new materials as well as to understand the physical mechanism of known superconductors. Density functional theory for superconductors (SCDFT)^{1,2} is one of the framework for such calculations; this method enables us to perform fully non-empirical simulations in the superconducting phases within a reasonable computational cost. The anisotropic Migdal-Eliashberg (ME) equations³ and the McMillan's formula^{4,5} which is the parametrization of the solution of the ME equations can also be used to estimate T_c . However, to solve the Migdal-Eliashberg equations⁶, we need to perform the summation of the Matsubara frequencies, and this summation requires a huge computational cost. Since the McMillan's formula involves an adjustable parameter to evaluate the effect of the Coulomb repulsion, the formula cannot compare the T_c s of a wide range of materials. In SCDFT, we can treat the electron-phonon interaction, the electron-electron repulsion, and the spin-fluctuation (SF)-mediated interaction⁷ in a first-principles manner. SCDFT has been applied to various kinds of materials such as elemental materials (Al, Nb, Mo, Ta, Pb)⁸, MgB₂⁹, graphite intercalations¹⁰, Li under high pressure¹¹, H₂ molecule solid¹², hydrogen compounds¹³, and FeSe¹⁴. On the other hand, the methodological improvements have also been proposed to include the anisotropic electron-phonon interaction, plasmons¹⁵, spin-fluctuation⁷, and the spin-orbit interaction (SOI)¹⁶.

However, the accuracy of the current approximated functional of SCDFT and the effects of the SOI and SF have not been verified systematically although such verification is highly desirable before we apply this method to a wide range of materials. Such a high-throughput calculation was performed, for examples, in the exploration of the low-thermal-conductivity compounds by using first-principles calculations together with the materi-

als informatics¹⁷. Such a benchmark is also useful to find a guideline for improving the theory and approximations of the superconducting density functional. For this purpose, we present benchmark calculations of SCDFT. As benchmark targets, we chose the simplest superconducting and non-superconducting materials, i.e., elemental materials; each material in this group consists of a single element. The computational cost is low for this group because most materials in this group contain only one or two atoms in the unit cell. Moreover, we can see the effects of the chemical difference as well as the strength of the SOI of each element.

This paper is organized as follows: In Sec. II we explain the formulation of SCDFT, including SF and SOI, and in Sec. III, detail of the implementation is shown. Then we show the result together with the numerical condition in Sec. IV, and discuss the results in Sec. V. Finally, we summarize the study in Sec. VI.

II. THEORY

In this section, we explain the detail of the SCDFT formulation including plasmon-aided mechanism¹⁵, SF effect⁷, and SOI¹⁶. We use the Hartree atomic units throughout the paper. In this study, we only consider the singlet superconductivity, while in Ref. 16, both the singlet- and triplet-superconducting states were considered. Within SCDFT, T_c is obtained as a temperature where the following Kohn-Sham superconducting gap $\Delta_{n\mathbf{k}}$ becomes zero at all the band n and wavenumber \mathbf{k} :

$$\Delta_{n\mathbf{k}} = -\frac{1}{2} \sum_{n'\mathbf{k}'} \frac{K_{n\mathbf{k}n'\mathbf{k}'}(\xi_{n\mathbf{k}}, \xi_{n'\mathbf{k}'})}{1 + Z_{n\mathbf{k}}(\xi_{n\mathbf{k}})} \times \frac{\Delta_{n'\mathbf{k}'}}{\sqrt{\xi_{n'\mathbf{k}'}^2 + \Delta_{n'\mathbf{k}'}^2}} \tanh\left(\frac{\sqrt{\xi_{n'\mathbf{k}'}^2 + \Delta_{n'\mathbf{k}'}^2}}{2T}\right), \quad (1)$$

where $\xi_{n\mathbf{k}}$ is the Kohn-Sham eigenvalue measured from the Fermi level at the band index n and wave-number

k. This non-linear gap equation (1) should be solved numerically at each temperature. The integration kernel $K_{n\mathbf{k}n'\mathbf{k}'}(\xi, \xi')$ indicates the superconducting-pair breaking and creating interaction and consists of the following three terms:

$$K_{n\mathbf{k}n'\mathbf{k}'}(\xi, \xi') \equiv K_{n\mathbf{k}n'\mathbf{k}'}^{ep}(\xi, \xi') + K_{n\mathbf{k}n'\mathbf{k}'}^{ee}(\xi, \xi') + K_{n\mathbf{k}n'\mathbf{k}'}^{sf}(\xi, \xi'), \quad (2)$$

namely, the electron-phonon, Coulomb repulsion, and spin-fluctuation kernel, respectively. On the other hand, the renormalization factor $Z_{n\mathbf{k}}(\xi_{n\mathbf{k}})$ consists of only the electron-phonon and the spin-fluctuation terms as

$$Z_{n\mathbf{k}}(\xi) \equiv Z_{n\mathbf{k}}^{ep}(\xi) + Z_{n\mathbf{k}}^{sf}(\xi), \quad (3)$$

because the Coulomb-repulsion contribution to this factor is already included in the Kohn-Sham eigenvalue $\xi_{n\mathbf{k}}$. The temperature T is defined by considering the Boltzmann constant $k_B = 1$.

Let us explain each term in the kernel and the renormalization factor below. The electron-phonon kernel K^{ep} and renormalization factor Z^{ep} are given by¹⁶

$$K_{n\mathbf{k}n'\mathbf{k}'}^{ep}(\xi, \xi') = \frac{2}{\tanh[\xi/(2T)] \tanh[\xi'/(2T)]} \sum_{\nu} |g_{n\mathbf{k}n'\mathbf{k}'}^{\nu}|^2 \times [I(\xi, \xi', \omega_{\mathbf{k}'-\mathbf{k}\nu}) - I(\xi, -\xi', \omega_{\mathbf{k}'-\mathbf{k}\nu})], \quad (4)$$

$$Z_{n\mathbf{k}}^{ep}(\xi) = \frac{-1}{\tanh[\xi/(2T)]} \sum_{n'\mathbf{k}'\nu} |g_{n\mathbf{k}n'\mathbf{k}'}^{\nu}|^2 \times [J(\xi, \xi_{n'\mathbf{k}'}, \omega_{\mathbf{k}'-\mathbf{k}\nu}) + J(\xi, -\xi_{n'\mathbf{k}'}, \omega_{\mathbf{k}'-\mathbf{k}\nu})], \quad (5)$$

where $\omega_{\mathbf{q}\nu}$ is the phonon frequency at the wave-number \mathbf{q} and branch ν . $I(\xi, \xi', \omega)$ and $J(\xi, \xi', \omega)$ are derived with the Kohn-Sham perturbation theory¹⁸, and are written as follows²:

$$I(\xi, \xi', \omega) = f_T(\xi) f_T(\xi') n_T(\omega) \times \left[\frac{e^{\xi/T} - e^{(\xi'+\omega)/T}}{\xi - \xi' - \omega} - \frac{e^{\xi'/T} - e^{(\xi+\omega)/T}}{\xi - \xi' + \omega} \right], \quad (6)$$

$$J(\xi, \xi', \omega) = \tilde{J}(\xi, \xi', \omega) - \tilde{J}(\xi, \xi', \omega), \quad (7)$$

$$\tilde{J}(\xi, \xi', \omega) = -\frac{f_T(\xi) + n_T(\xi)}{\xi - \xi' - \omega} \times \left[\frac{f_T(\xi') - f_T(\xi - \omega)}{\xi - \xi' - \omega} - \frac{f_T(\xi - \omega) f_T(-\xi' + \omega)}{T} \right], \quad (8)$$

where $f_T(\xi)$ and $n_T(\omega)$ are the Fermi-Dirac and the Bose-Einstein distribution function, respectively. The functions $I(\xi, \xi', \omega)$ and $J(\xi, \xi', \omega)$ yield a temperature-dependent retardation effect. The electron-phonon vertex g between Kohn-Sham orbitals indexed with (n, \mathbf{k}) and $(n', \mathbf{k} + \mathbf{q})$, and the phonon (\mathbf{q}, ν) is computed as¹⁹

$$g_{n\mathbf{k}n'\mathbf{k}+\mathbf{q}}^{\nu} = \int d^3r \sum_{\sigma\sigma'} \varphi_{n'\mathbf{k}+\mathbf{q}\sigma}^*(\mathbf{r}) \varphi_{n\mathbf{k}\sigma}(\mathbf{r})$$

$$\times \sum_{\tau} \frac{\boldsymbol{\eta}_{\mathbf{q}\nu}^{\tau} \cdot \boldsymbol{\delta}^{\mathbf{q}\tau} V_{\sigma\sigma'}^{\text{KS}}(\mathbf{r})}{\sqrt{M_{\tau} \omega_{\mathbf{q}\nu}}}, \quad (9)$$

where M_{τ} is the mass of atom labeled by τ , $\boldsymbol{\eta}_{\mathbf{q}\nu}^{\tau}$ is the polarization vector of phonon (\mathbf{q}, ν) and atom τ , $\varphi_{n\mathbf{k}\sigma}(\mathbf{r})$ is the σ component of the spinor Kohn-Sham orbital at (n, \mathbf{k}) , and $\boldsymbol{\delta}^{\mathbf{q}\tau} V_{\sigma\sigma'}^{\text{KS}}(\mathbf{r})$ is the Kohn-Sham potential deformed by the periodic displacement of atom τ and wave number \mathbf{q} . This deformation potential is obtained during the phonon calculation based on density functional perturbation theory (DFPT)²⁰. The electron-phonon kernel K^{ep} is always negative. Therefore it has a positive contribution to form the Cooper pair. On the other hand, the electron-phonon renormalization factor Z^{ep} weakens the effect by the kernels.

The electron-electron repulsion kernel K^{ee} in Eq. (2) is¹⁶

$$K_{n\mathbf{k}n'\mathbf{k}'}^{ee}(\xi, \xi') = \frac{2}{\pi} \int_0^{\infty} d\omega \frac{|\xi| + |\xi'|}{(|\xi| + |\xi'|)^2 + \omega^2} V_{n\mathbf{k}n'\mathbf{k}'}^{ee}(i\omega), \quad (10)$$

where $V_{n\mathbf{k}n'\mathbf{k}'}^{ee}(i\omega)$ is the dynamically screened exchange integral between the Kohn-Sham orbitals (n, \mathbf{k}) and (n', \mathbf{k}')

$$V_{n\mathbf{k}n'\mathbf{k}'}^{ee}(i\omega) = \iint d^3r d^3r' V_{RPA}(\mathbf{r}, \mathbf{r}', i\omega) \times \rho_{n\mathbf{k}n'\mathbf{k}'}^{(0)}(\mathbf{r}) \rho_{n\mathbf{k}n'\mathbf{k}'}^{(0)*}(\mathbf{r}'), \quad (11)$$

$$\rho_{n\mathbf{k}n'\mathbf{k}'}^{(0)}(\mathbf{r}) = \sum_{\sigma} \varphi_{n\mathbf{k}\sigma}^*(\mathbf{r}) \varphi_{n'\mathbf{k}'\sigma}(\mathbf{r}). \quad (12)$$

In this study, the screened Coulomb interaction V_{RPA} is computed within the random phase approximation (RPA)²¹ as

$$V_{RPA}(\mathbf{r}, \mathbf{r}', i\omega) = \frac{1}{|\mathbf{r} - \mathbf{r}'|} + \iint d^3r_1 d^3r_2 \times V_{RPA}(\mathbf{r}, \mathbf{r}_1, i\omega) \Pi_{\text{KS}}^{00}(\mathbf{r}_1, \mathbf{r}_2, i\omega) \frac{1}{|\mathbf{r}_2 - \mathbf{r}'|}, \quad (13)$$

where Π_{KS}^{00} is the electronic susceptibility of the Kohn-Sham system (the non-perturbed susceptibility). This electronic susceptibility is a component of the following susceptibilities of the Kohn-Sham system:

$$\Pi_{\text{KS}}^{\alpha\alpha}(\mathbf{r}, \mathbf{r}', i\omega) = \sum_{\mathbf{k}\mathbf{k}'n'n'} \frac{\theta(-\xi_{n\mathbf{k}}) - \theta(-\xi_{n'\mathbf{k}'})}{\xi_{n\mathbf{k}} - \xi_{n'\mathbf{k}'} + i\omega} \times \rho_{n\mathbf{k}n'\mathbf{k}'}^{(\alpha)}(\mathbf{r}) \rho_{n\mathbf{k}n'\mathbf{k}'}^{(\alpha)*}(\mathbf{r}'), \quad (14)$$

where α takes 0, x , y , z , and

$$\rho_{n\mathbf{k}n'\mathbf{k}'}^{(x)}(\mathbf{r}) = \sum_{\sigma} \varphi_{n\mathbf{k}\sigma}^*(\mathbf{r}) \varphi_{n'\mathbf{k}'-\sigma}(\mathbf{r}), \quad (15)$$

$$\rho_{n\mathbf{k}n'\mathbf{k}'}^{(y)}(\mathbf{r}) = \sum_{\sigma} \sigma \varphi_{n\mathbf{k}\sigma}^*(\mathbf{r}) \varphi_{n'\mathbf{k}'-\sigma}(\mathbf{r}), \quad (16)$$

$$\rho_{n\mathbf{k}n'\mathbf{k}'}^{(z)}(\mathbf{r}) = \sum_{\sigma} \sigma \varphi_{n\mathbf{k}\sigma}^*(\mathbf{r}) \varphi_{n'\mathbf{k}'\sigma}(\mathbf{r}). \quad (17)$$

The spin susceptibility Π_{KS}^{xx} , Π_{KS}^{yy} , and Π_{KS}^{zz} are used in the spin-fluctuation term later on. Because of the factor $[\theta(-\xi_{n\mathbf{k}}) - \theta(-\xi_{n'\mathbf{k}'})]/(\xi_{n\mathbf{k}} - \xi_{n'\mathbf{k}'} + i\omega)$, these susceptibilities are affected largely by the electronic states in the vicinity of Fermi surfaces.

We propose the spin-fluctuation (SF) kernel K^{sf} in Eq. (2) and the renormalization Z^{sf} in Eq. (3) constructed by using the noncollinear spinor wavefunctions. The following formulation is an extension of those quantities in the collinear magnetism¹⁴.

$$K_{n\mathbf{k}n'\mathbf{k}'}^{sf}(\xi, \xi') = \frac{2}{\pi} \int_0^\infty d\omega \frac{|\xi| + |\xi'|}{(|\xi| + |\xi'|)^2 + \omega^2} \times \Lambda_{n\mathbf{k}n'\mathbf{k}'}^{sf}(i\omega), \quad (18)$$

$$Z_{n\mathbf{k}}^{sf}(\xi) = \frac{1}{\pi} \sum_{n'\mathbf{k}'} \int_0^\infty d\omega \frac{(|\xi| + |\xi_{n'\mathbf{k}'}|)^2 - \omega^2}{[(|\xi| + |\xi_{n'\mathbf{k}'}|)^2 + \omega^2]^2} \times \Lambda_{n\mathbf{k}n'\mathbf{k}'}^{sf}(i\omega), \quad (19)$$

where

$$\Lambda_{n\mathbf{k}n'\mathbf{k}'}^{sf}(i\omega) = \sum_{\alpha=x,y,z} \iint d^3r d^3r' \Lambda_{\alpha\alpha}^{sf}(\mathbf{r}, \mathbf{r}', i\omega) \times \rho_{n\mathbf{k}n'\mathbf{k}'}^{(\alpha)}(\mathbf{r}) \rho_{n\mathbf{k}n'\mathbf{k}'}^{(\alpha)*}(\mathbf{r}'). \quad (20)$$

$\Lambda_{n\mathbf{k}n'\mathbf{k}'}^{sf}$ has a similar form to the screened exchange integral of Eq. (11), and it involves the summation over the components x, y , and z components of the following SF-mediated interaction:

$$\Lambda_{\alpha\alpha}^{sf}(\mathbf{r}, \mathbf{r}', i\omega) = - \iint d^3r_1 d^3r_2 \times I_{XC}^{\alpha\alpha}(\mathbf{r}, \mathbf{r}_1) \Pi^{\alpha\alpha}(\mathbf{r}_1, \mathbf{r}_2, i\omega) I_{XC}^{\alpha\alpha}(\mathbf{r}_2, \mathbf{r}'), \quad (21)$$

where $\Pi^{\alpha\alpha}$ is the spin susceptibility of the interacting system as²²

$$\Pi^{\alpha\alpha}(\mathbf{r}, \mathbf{r}', i\omega) = \Pi_{\text{KS}}^{\alpha\alpha}(\mathbf{r}, \mathbf{r}', i\omega) + \iint d^3r_1 d^3r_2 \times \Pi^{\alpha\alpha}(\mathbf{r}, \mathbf{r}_1, i\omega) I_{XC}^{\alpha\alpha}(\mathbf{r}_1, \mathbf{r}_2) \Pi_{\text{KS}}^{\alpha\alpha}(\mathbf{r}_2, \mathbf{r}', i\omega). \quad (22)$$

In Eqs. (21) and (22), the spin-spin interaction is included through the exchange correlation kernel:

$$I_{XC}^{\alpha\alpha}(\mathbf{r}, \mathbf{r}') \equiv \frac{\delta^2 E_{XC}}{\delta m_\alpha(\mathbf{r}) \delta m_\alpha(\mathbf{r}')} \quad (23)$$

which is the second-order functional derivative of the exchange correlation energy with respect to the spin density along the α direction, m_α . These quantities are computed from the result of the standard density functional calculations of the normal (non-superconducting) state. Therefore we compute T_c by solving the gap equation (1) as a post-process of those calculations. This treatment so-called the decoupling approximation is reliable when the energy scales of the bandwidth and the superconducting gap are largely different².

III. IMPLEMENTATION

In this section, we explain the practical procedure to perform the calculations explained in the previous section.

A. Evaluation of exchange integrals with Fourier transformation

The exchange integrals with Coulomb interaction part $V_{n\mathbf{k}n'\mathbf{k}'}^{ee}$ of Eq. (11) and the SF part $\Lambda_{n\mathbf{k}n'\mathbf{k}'}^{sf}$ of Eq. (20) can be computed efficiently by using the Fourier transformation as follows: First $\rho^{(\alpha)}(\mathbf{r})$ in Eqs. (12) and (15)-(17) has the periodicity of the lattice vector \mathbf{R} together with the phase factor from the Bloch theorem as

$$\rho_{n\mathbf{k}n'\mathbf{k}'}^{(\alpha)}(\mathbf{r} + \mathbf{R}) = e^{i(\mathbf{k}' - \mathbf{k}) \cdot \mathbf{R}} \rho_{n\mathbf{k}n'\mathbf{k}'}^{(\alpha)}(\mathbf{r}). \quad (24)$$

Therefore $\rho^{(\alpha)}(\mathbf{r})$ can be expanded with the Fourier components of the reciprocal lattice vectors \mathbf{G} as

$$\rho_{n\mathbf{k}n'\mathbf{k}+\mathbf{q}}^{(\alpha)}(\mathbf{r}) = \sum_{\mathbf{G}} e^{i(\mathbf{q}+\mathbf{G}) \cdot \mathbf{r}} \tilde{\rho}_{n\mathbf{k}n'\mathbf{k}+\mathbf{q}}^{(\alpha)}(\mathbf{G}), \quad (25)$$

where $\tilde{\rho}^{(\alpha)}(\mathbf{G})$ is defined by the Fourier transformation of $\rho^{(\alpha)}(\mathbf{r})$ as follows:

$$\tilde{\rho}_{n\mathbf{k}n'\mathbf{k}+\mathbf{q}}^{(\alpha)}(\mathbf{G}) \equiv \frac{1}{v_{\text{uc}}} \int_{\text{uc}} d^3r e^{-i(\mathbf{q}+\mathbf{G}) \cdot \mathbf{r}} \rho_{n\mathbf{k}n'\mathbf{k}+\mathbf{q}}^{(\alpha)}(\mathbf{r}). \quad (26)$$

Then the exchange integral of Eq. (11) is rewritten as

$$V_{n\mathbf{k}n'\mathbf{k}+\mathbf{q}}^{ee}(i\omega) = \sum_{\mathbf{G}\mathbf{G}'} V_{RPA}^{\mathbf{q}}(\mathbf{G}, \mathbf{G}', i\omega) \times \tilde{\rho}_{n\mathbf{k}n'\mathbf{k}+\mathbf{q}}^{(0)}(\mathbf{G}) \tilde{\rho}_{n\mathbf{k}n'\mathbf{k}+\mathbf{q}}^{(0)*}(\mathbf{G}'), \quad (27)$$

where $V_{RPA}^{\mathbf{q}}$ is the Fourier component of the screened Coulomb interaction as follows:

$$V_{RPA}^{\mathbf{q}}(\mathbf{G}, \mathbf{G}', i\omega) \equiv \iint d^3r d^3r' e^{i(\mathbf{q}+\mathbf{G}) \cdot \mathbf{r}} e^{-i(\mathbf{q}+\mathbf{G}') \cdot \mathbf{r}'} V_{RPA}(\mathbf{r}, \mathbf{r}', i\omega). \quad (28)$$

However, we do not need to know $V_{RPA}(\mathbf{r}, \mathbf{r}', i\omega)$ itself, since we show that we can compute $V_{RPA}^{\mathbf{q}}(\mathbf{G}, \mathbf{G}', i\omega)$ at each \mathbf{q} separately with the help of the Bloch theorem as shown below. By substituting $V_{RPA}(\mathbf{r}, \mathbf{r}', i\omega)$ of Eq. (13) into Eq. (28), we obtain

$$V_{RPA}^{\mathbf{q}}(\mathbf{G}, \mathbf{G}', i\omega) = \frac{4\pi \delta_{\mathbf{G}\mathbf{G}'}}{|\mathbf{q} + \mathbf{G}|^2} + \sum_{\mathbf{G}_1} V_{RPA}^{\mathbf{q}}(\mathbf{G}, \mathbf{G}_1, i\omega) \Pi_{\text{KS}}^{00\mathbf{q}}(\mathbf{G}_1, \mathbf{G}', i\omega) \frac{4\pi}{|\mathbf{q} + \mathbf{G}'|^2} = \left[\frac{|\mathbf{q} + \mathbf{G}'|^2 \delta_{\mathbf{G}\mathbf{G}'}}{4\pi} - \Pi_{\text{KS}}^{00\mathbf{q}}(\mathbf{G}, \mathbf{G}', i\omega) \right]^{-1}, \quad (29)$$

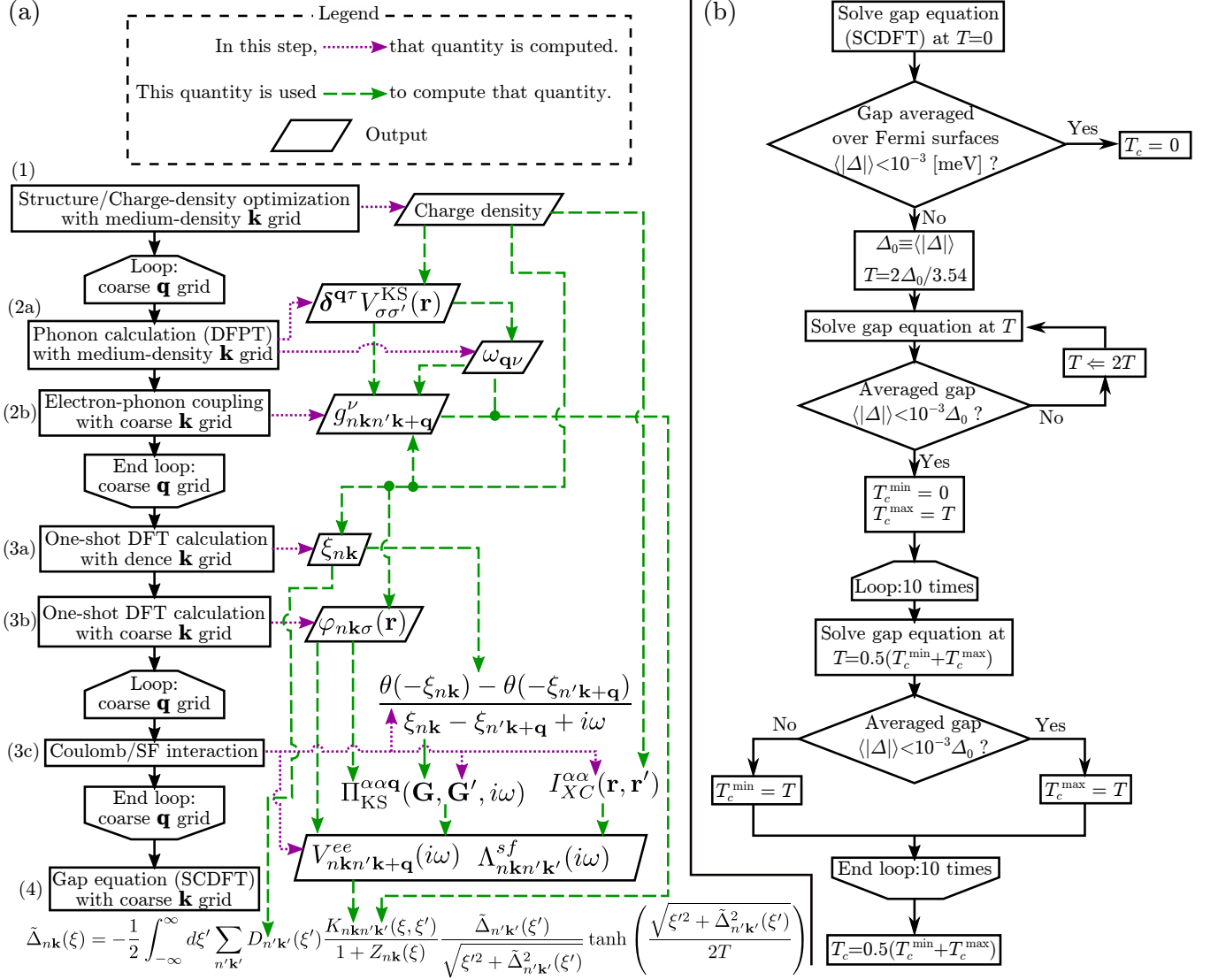


FIG. 1. (a) The flow chart to perform the SCDF calculation for each material in this study. The indices of steps are the same as those written in Sec. III D. (b) The flow chart of the bisection method used to compute T_c .

where $\Pi_{KS}^{\alpha\alpha\mathbf{q}}(\mathbf{G}, \mathbf{G}', i\omega)$ is the Fourier component of the susceptibilities of the Kohn-Sham system of Eq. (14) given by

$$\begin{aligned} \Pi_{KS}^{\alpha\alpha\mathbf{q}}(\mathbf{G}, \mathbf{G}', i\omega) &\equiv \iint d^3r d^3r' e^{i(\mathbf{q}+\mathbf{G})\cdot\mathbf{r}} e^{-i(\mathbf{q}+\mathbf{G}')\cdot\mathbf{r}'} \Pi_{KS}^{\alpha\alpha}(\mathbf{r}, \mathbf{r}', i\omega) \\ &= \sum_{\mathbf{k}n\mathbf{k}'} \frac{\theta(-\xi_{n\mathbf{k}}) - \theta(-\xi_{n'\mathbf{k}+\mathbf{q}})}{\xi_{n\mathbf{k}} - \xi_{n'\mathbf{k}+\mathbf{q}} + i\omega} \tilde{\rho}_{n\mathbf{k}n'\mathbf{k}+\mathbf{q}}^{(\alpha)}(\mathbf{G}) \tilde{\rho}_{n\mathbf{k}n'\mathbf{k}+\mathbf{q}}^{(\alpha)*}(\mathbf{G}'). \end{aligned} \quad (30)$$

In the derivation of Eq. (29), we used the periodicity of each term with respect to the lattice vector. The factor $[\theta(-\xi_{n\mathbf{k}}) - \theta(-\xi_{n'\mathbf{k}+\mathbf{q}})]/(\xi_{n\mathbf{k}} - \xi_{n'\mathbf{k}+\mathbf{q}} + i\omega)$ in the susceptibilities varies rapidly in the vicinity of Fermi surfaces, and we need a dense \mathbf{k} grid to compute it accu-

rately, which may require a huge numerical cost. Therefore we use the reverse interpolation scheme explained in Sec. III.C.1 of Ref. 23. In this scheme, we compute the explicitly energy-dependent factor with a dense \mathbf{k} grid while we compute the other parts by using a coarse \mathbf{k} grid because $\tilde{\rho}_{n\mathbf{k}n'\mathbf{k}+\mathbf{q}}^{(\alpha)}(\mathbf{G})$ varies more smoothly than the energy-dependent factor. The SF term can be computed in the same manner at each \mathbf{q} separately. The Fourier component of the SF-mediated interaction of Eq. (21) is

$$\begin{aligned} \Lambda_{\mathbf{q}}^{sf, \alpha\alpha}(\mathbf{G}, \mathbf{G}', i\omega) &= - \sum_{\mathbf{G}_1, \mathbf{G}_2} I_{XC}^{\alpha\alpha\mathbf{q}}(\mathbf{G}, \mathbf{G}_1) \\ &\times \left[(\Pi_{KS}^{\alpha\alpha\mathbf{q}}(\mathbf{G}_1, \mathbf{G}_2))^{-1} - I_{XC}^{\alpha\alpha\mathbf{q}}(\mathbf{G}_1, \mathbf{G}_2) \right]^{-1} I_{XC}^{\alpha\alpha\mathbf{q}}(\mathbf{G}_2, \mathbf{G}'), \end{aligned} \quad (31)$$

where $I_{XC}^{\alpha\alpha\mathbf{q}}$ is the Fourier component of the exchange correlation kernel of Eq. (23). If we use the local density approximation (LDA) for this kernel, $I_{XC}^{\alpha\alpha\mathbf{q}}(\mathbf{G}, \mathbf{G}')$ does not depend on \mathbf{q} , and this is what we employ in the study. This is equivalent to the adiabatic local density approximation (ALDA)²² in time-dependent density functional theory²⁴.

B. Auxiliary gap equation

The gap equation (1) is solved with the auxiliary energy axis²³ to capture the rapid change of the explicitly energy-dependent function in the vicinity of Fermi surfaces. In this method, the gap function $\Delta_{n\mathbf{k}}$ depends also on the auxiliary energy; the auxiliary gap function $\tilde{\Delta}_{n\mathbf{k}}(\xi)$ satisfies $\tilde{\Delta}_{n\mathbf{k}}(\xi_{n\mathbf{k}}) = \Delta_{n\mathbf{k}}$. Then, the gap equation (1) becomes

$$\tilde{\Delta}_{n\mathbf{k}}(\xi) = -\frac{1}{2} \int_{-\infty}^{\infty} d\xi' \sum_{n'\mathbf{k}'} D_{n'\mathbf{k}'}(\xi') \frac{K_{n\mathbf{k}n'\mathbf{k}'}(\xi, \xi')}{1 + Z_{n\mathbf{k}}(\xi)} \times \frac{\tilde{\Delta}_{n'\mathbf{k}'}(\xi')}{\sqrt{\xi'^2 + \tilde{\Delta}_{n'\mathbf{k}'}^2(\xi')}} \tanh\left(\frac{\sqrt{\xi'^2 + \tilde{\Delta}_{n'\mathbf{k}'}^2(\xi')}}{2T}\right), \quad (32)$$

where $D_{n\mathbf{k}}(\xi)$ is the (n, \mathbf{k}) -resolved density of states. With the same manner, the electron-phonon and SF renormalization factors of Eqs. (5) and (19) become

$$Z_{n\mathbf{k}}^{ep}(\xi) = \frac{-1}{\tanh[\xi/(2T)]} \int_{-\infty}^{\infty} d\xi' \sum_{n'\mathbf{k}'\nu} D_{n'\mathbf{k}'}(\xi') |g_{n\mathbf{k}n'\mathbf{k}'}^\nu|^2 \times [J(\xi, \xi', \omega_{\mathbf{k}'-\mathbf{k}\nu}) + J(\xi, -\xi', \omega_{\mathbf{k}'-\mathbf{k}\nu})] \quad (33)$$

and

$$Z_{n\mathbf{k}}^{sf}(\xi) = \frac{1}{\pi} \int_{-\infty}^{\infty} d\xi' \sum_{n'\mathbf{k}'} D_{n'\mathbf{k}'}(\xi') \int_0^{\infty} d\omega \times \frac{(|\xi| + |\xi_{n'\mathbf{k}'}|)^2 - \omega^2}{[(|\xi| + |\xi_{n'\mathbf{k}'}|)^2 + \omega^2]^2} \Lambda_{n\mathbf{k}n'\mathbf{k}'}^{sf}(i\omega), \quad (34)$$

respectively, where the reverse interpolation method is employed again; the (n, \mathbf{k}) -resolved density of states $D_{n\mathbf{k}}(\xi)$ is computed with the dense \mathbf{k} grid, while the other parts are computed on the coarse \mathbf{k} grid, then we combine them.

C. Frequency integral

The integration in Eq. (10) involves the frequency ω spanning $[0, \infty]$. Therefore, to perform this integration numerically, we change the variable as follows:

$$\omega = (|\xi| + |\xi'|) \frac{1+x}{1-x}. \quad (35)$$

Then Eq. (10) becomes

$$K_{n\mathbf{k}n'\mathbf{k}'}^{ee}(\xi, \xi') = \frac{2}{\pi} \int_{-1}^1 dx \frac{1}{1+x^2} \times V_{n\mathbf{k}n'\mathbf{k}'}^{ee} \left(i(|\xi| + |\xi'|) \frac{1+x}{1-x} \right). \quad (36)$$

When $|\xi| + |\xi'| = 0$, this integration becomes $V_{n\mathbf{k}n'\mathbf{k}'}^{ee}(0)$. To obtain $V_{n\mathbf{k}n'\mathbf{k}'}^{ee}(i\omega)$ at an arbitrary ω , we first compute $V_{n\mathbf{k}n'\mathbf{k}'}^{ee}(i\omega)$ at discrete non-uniform points $\omega = 0, \omega_1, \omega_2, \dots, \infty$ and interpolate them. By using the same transformation as in Eq. (35), the frequency integral in the SF renormalization term (34) is performed as follows:

$$Z_{n\mathbf{k}}^{sf}(\xi) = \frac{1}{\pi} \int_{-\infty}^{\infty} d\xi' \sum_{n'\mathbf{k}'} D_{n'\mathbf{k}'}(\xi') \int_{-1}^1 dx \frac{-2x}{(|\xi| + |\xi_{n'\mathbf{k}'}|)(1+x^2)^2} \times \Lambda_{n\mathbf{k}n'\mathbf{k}'}^{sf} \left(i(|\xi| + |\xi'|) \frac{1+x}{1-x} \right). \quad (37)$$

The numerical integration with respect to the variable x ranging $[-1, 1]$ can be performed by using the Gauss quadrature.

D. Overall procedure

Figure 1 (a) shows the calculation flow. We employ the following three different wavenumber grids to perform Brillouin-zone integrals efficiently:

coarse grid: To reduce the computational cost, we use a coarse grid for the wavenumber \mathbf{q} of phonons and susceptibilities. The grid is shifted with a half of the grid to avoid the singularity at the Γ point. The grid is also used for solving the gap equation.

medium-density grid: The atomic structure and the charge density are optimized with the self-consistent field calculation by using \mathbf{k} grid denser than the coarse grid. This \mathbf{k} grid is also used for electronic states in the DFPT calculation.

dense grid: To treat the explicitly energy-dependent factor in the calculations of susceptibilities and the (n, \mathbf{k}) -dependent density of states in the gap equation (32), a dense \mathbf{k} grid is employed.

The overall calculations are performed as follows:

1. First, we optimize the atomic structure and the charge density by using the standard density functional calculation with the medium-density \mathbf{k} grid. The following calculation is performed on this optimized atomic structure and with the charge density.
2. We compute the electron-phonon interaction and the frequency of phonons whose wavenumber \mathbf{q} is on the coarse grid with a half-grid shift. This step is separated into the following two sub-steps:

- (a) The phonon calculation based on DFPT is performed. The electronic states used in this calculation have a wavenumber \mathbf{k} on the medium-density grid.
 - (b) Electron-phonon vertex of Eq. (9) between the Kohn-Sham orbitals (n, \mathbf{k}) and $(n', \mathbf{k} + \mathbf{q})$ is computed, where the wavenumber \mathbf{k} is on the coarse grid.
3. Next, we compute the exchange integrals of screened Coulomb and SF-mediated interaction whose transitional momentum \mathbf{q} is on the coarse grid with a half-grid shift. This step is separated into the following three sub-steps:
- (a) One-shot DFT calculation on the dense \mathbf{k} grid is performed. The resulting energy dispersion $\xi_{n\mathbf{k}}$ is used later to compute the explicitly energy-dependent term in the susceptibilities.
 - (b) One-shot DFT calculation on the coarse \mathbf{k} grid with and without a half-grid shift is performed. The resulting Kohn-Sham orbitals will be used to compute $\rho^{(\alpha)}(\mathbf{r})$ of Eqs. (12) and (15)-(17).
 - (c) The exchange integrals of screened Coulomb and SF-mediated interaction between the Kohn-Sham orbitals (n, \mathbf{k}) and $(n', \mathbf{k} + \mathbf{q})$ are computed, where the wavenumber \mathbf{k} is on the coarse grid.
4. The gap equation within SCDFPT is solved on the coarse \mathbf{k} grid at each temperature. Then T_c is obtained as a minimum temperature where all $\Delta_{n\mathbf{k}}(\xi)$ vanish.

The transition temperature T_c is found by using the bisection method shown in Fig. 1 (b). While the initial lower limit of T_c is set to zero, the initial upper limit is set to the T_c estimated by the Bardeen-Cooper-Schrieffer theory^{25,26} ($2\Delta_0/3.54$, where Δ_0 is the superconducting gap averaged over Fermi surfaces at zero kelvin). If there is a finite gap even at this upper limit, although it hardly occurs, we double the initial upper limit. Then we repeat the bisection step ten times and find T_c .

IV. RESULT

In this section we first explain the numerical condition of this study, then show the result of the benchmark.

The numerical condition is as follows: We use the DFT code QUANTUM ESPRESSO²⁷ which employs plane waves and pseudopotentials. Perdew-Burke-Ernzerhof's density functional²⁸ based on generalized gradient approximation is used. We use the optimized norm-conserving pseudopotential²⁹ library provided by Schlipf-Gygi (SG15)^{30,31}. The energy cutoff for the charge density of each element is specified by using the criteria

TABLE I. Structure, cutoff for the plane wave for charge density, \mathbf{q} -grid for phonon, and the error of the lattice constant $\langle \Delta a/a_{\text{exp}} \rangle \equiv (V_{\text{calc}}/V_{\text{exp}})^{1/3} - 1$. V_{calc} and V_{exp} are the calculated and experimental unit-cell volume, respectively.

	structure	cutoff [Ry]	coarse grid	$\langle \Delta a/a_{\text{exp}} \rangle$ [%]
Be	hcp	65	$10 \times 10 \times 5$	-0.74
Na	bcc	90	$6 \times 6 \times 6$	-0.60
Mg	hcp	65	$7 \times 7 \times 4$	-0.77
Al	fcc	65	$8 \times 8 \times 8$	-0.90
K	bcc	120	$5 \times 5 \times 5$	0.61
Ca	fcc	120	$6 \times 6 \times 6$	-1.20
Sc	hcp	45	$7 \times 7 \times 4$	-0.49
Ti	hcp	50	$7 \times 7 \times 4$	-0.28
V	bcc	40	$9 \times 9 \times 9$	-1.19
Cu	fcc	90	$9 \times 9 \times 9$	0.42
Zn	hcp	90	$8 \times 8 \times 4$	-0.02
Ga	α -Ga	150	$5 \times 5 \times 4$	1.35
Rb	bcc	30	$5 \times 5 \times 5$	0.58
Sr	fcc	30	$5 \times 5 \times 5$	-1.09
Y	hcp	40	$6 \times 6 \times 3$	0.94
Zr	hcp	50	$7 \times 7 \times 4$	0.09
Nb	bcc	90	$8 \times 8 \times 8$	0.53
Mo	bcc	35	$8 \times 8 \times 8$	0.44
Tc	hcp	30	$8 \times 8 \times 4$	0.04
Ru	hcp	35	$8 \times 8 \times 4$	-0.62
Rh	fcc	35	$8 \times 8 \times 8$	0.73
Pd	fcc	45	$8 \times 8 \times 8$	1.18
Ag	fcc	50	$8 \times 8 \times 8$	1.42
Cd	hcp	45	$7 \times 7 \times 3$	2.32
In	bct	65	$7 \times 7 \times 7$	1.84
Sn	β -Sn	50	$7 \times 7 \times 7$	1.72
Cs	bcc	75	$4 \times 4 \times 4$	1.01
Ba	bcc	30	$5 \times 5 \times 5$	-0.19
La	hcp	120	$6 \times 6 \times 3$	0.60
Hf	hcp	55	$7 \times 7 \times 4$	0.01
Ta	bcc	50	$8 \times 8 \times 8$	0.79
W	bcc	50	$8 \times 8 \times 8$	0.62
Re	hcp	60	$8 \times 8 \times 4$	0.39
Os	hcp	55	$8 \times 8 \times 4$	1.00
Ir	fcc	40	$8 \times 8 \times 8$	1.29
Pt	fcc	60	$8 \times 8 \times 8$	1.15
Au	fcc	45	$8 \times 8 \times 8$	1.15
Hg	trigonal	50	$6 \times 6 \times 6$	6.81
Tl	hcp	55	$6 \times 6 \times 3$	3.10
Pb	fcc	35	$6 \times 6 \times 6$	1.77

and the convergence profiles in the Standard Solid State Pseudopotentials³¹. To perform the Brillouin-zone integration, we employ the optimized tetrahedron method³². The number of grids along each reciprocal lattice vector is proportional to the length of that vector. Table I shows these conditions for each element. The SCDFPT calculation is performed by using the program package SUPERCONDUCTING TOOLKIT³³. We set the medium-density grid twice the coarse grid and set the dense grid twice the medium-density grid. For example, 8^3 , 16^3 , and 32^3 grids are used for the coarse, medium-density, and dense grids, respectively, for Al. The minimum scale of the non-uniform auxiliary energy grid used in the gap equation

(32) is set to 10^{-7} Ry. In the calculation of the magnetic exchange-correlation kernel of Eq. (23), we ignore the gradient correction. For stabilizing the phonon calculation, the lattice constants and the internal atomic coordinates are optimized; The optimized lattice constants are listed in Tbl. I. To compute the susceptibilities in Eq. (30) and solve the gap equation (32), we include $40 \times N_{\text{atom}}$ ($20 \times N_{\text{atom}}$) empty bands for the calculation with (without) SOI, where N_{atom} is the number of atoms per unit cell.

Next, we move onto the result. Figure 2 shows the experimental T_c (T_c^{exp})³⁴, the theoretical T_c computed with and without SOI/SF in a periodic-table form. Also, to examine the effects of the electron-phonon interaction, the screened Coulomb repulsion, and the spin-fluctuation, we show the following quantities in the same figure: The density of states (DOS) at the Fermi level divided by the number of atoms indicates the number of states interacting with a state; this quantity affects the strength of the mean-field. Fröhlich's mass-enhancement parameter

$$\lambda = \sum_{\mathbf{q}\nu} \lambda_{\mathbf{q}\nu}, \quad (38)$$

and the averaged phonon frequencies

$$\omega_{\text{ln}} = \exp \left[\frac{1}{\lambda} \sum_{\mathbf{q}\nu} \lambda_{\mathbf{q}\nu} \ln(\omega_{\mathbf{q}\nu}) \right], \quad (39)$$

appear in the conventional McMillan formula^{4,5}

$$T_c = \frac{\omega_{\text{ln}}}{1.2} \exp \left[\frac{-1.04(1 + \lambda)}{\lambda - \mu^*(1 + 0.62\lambda)} \right] \quad (40)$$

which has been used to estimate T_c semi-empirically with an adjustable parameter μ^* . The (\mathbf{q}, ν) -dependent mass-enhancement parameter $\lambda_{\mathbf{q}\nu}$ is computed as follows:

$$\lambda_{\mathbf{q}\nu} = \frac{2}{D(0)\omega_{\mathbf{q}\nu}} \sum_{\mathbf{k}n'n'} |g_{n\mathbf{k}n'\mathbf{k}+\mathbf{q}}^\nu|^2 \delta(\xi_{n\mathbf{k}}) \delta(\xi_{n'\mathbf{k}+\mathbf{q}}), \quad (41)$$

where $D(0)$ is the density of states at the Fermi level. We perform the Brillouin-zone integral, including two delta functions, by using the dense \mathbf{k} grid together with the optimized tetrahedron method³². Because of the double delta function $\delta(\xi_{n\mathbf{k}})\delta(\xi_{n'\mathbf{k}+\mathbf{q}})$, this summation involves the electron-phonon vertices only between the electronic states at the Fermi level. Therefore, the Fröhlich's mass-enhancement parameter λ in Eq. (38) indicates the retarded phonon-mediated interaction ($2|g|^2/\omega$) averaged over Fermi surfaces times the density of state at the Fermi level. Similarly, ω_{ln} indicates the typical frequency of phonons which couples largely with the electronic states at the Fermi level. Therefore, λ and ω_{ln} closely relate to the electron-phonon contribution to T_c . In an analogous fashion to λ , we show parameters for the Coulomb repulsion and SF as

$$\mu_C = \frac{1}{D(0)} \sum_{\mathbf{k}\mathbf{k}'nn'} K_{n\mathbf{k}n'\mathbf{k}'}^{ee} \delta(\xi_{n\mathbf{k}}) \delta(\xi_{n'\mathbf{k}'}), \quad (42)$$

and

$$\mu_s = \frac{1}{D(0)} \sum_{\mathbf{k}\mathbf{k}'nn'} K_{n\mathbf{k}n'\mathbf{k}'}^{sf} \delta(\xi_{n\mathbf{k}}) \delta(\xi_{n'\mathbf{k}'}), \quad (43)$$

respectively. These parameters are the Coulomb [Eq.(10)] and SF [Eq.(18)] kernels averaged over Fermi surfaces times the density of states at the Fermi level.

We note that in Fig. (2), some results are absent because of the following reason: Li has a huge unit cell at a low temperature, and it is computationally demanding. Cr, Mn, Fe, Co, and Ni show a magnetic order at the low temperature. Therefore, the formalism of the spin-fluctuation (21) used in this study breaks down; the matrix

$$\delta_{\mathbf{G}\mathbf{G}'} - \sum_{\mathbf{G}_1} \Pi_{\text{KS}}^{\alpha\alpha\mathbf{q}}(\mathbf{G}, \mathbf{G}_1) I_{XC}^{\alpha\alpha\mathbf{q}}(\mathbf{G}_1, \mathbf{G}') \quad (44)$$

does not become positive definite (the Stoner's criterion) for those materials. For Be and Ba, there is no pseudopotential together with SOI in the pseudopotential library used in this study. Since we try to unify the condition of the calculation for all elements, we leave the result of these two materials together with SOI blank. For Y, Zr, In (with SOI), La, Hf, and Hg, we obtained imaginary phonon frequencies because of an artificial long-range structure instability. For such cases, we could not continue the calculation because of the breakdown of the formulations of the electron-phonon kernel [Eq. (4)] and renormalization term [Eq. (5)]. Therefore, we leave the results for those cases blank.

V. DISCUSSION

In this section, we discuss the result shown in the previous section. To check the accuracy of the calculation of the electron-phonon interaction, we plot in Fig. 3 the calculated- and experimental-³⁵ Sommerfeld coefficient γ_S which is the prefactor of the specific heat at a low temperature

$$C_v = \gamma_S T + O(T^3). \quad (45)$$

This coefficient is estimated by using the density of states and the Fröhlich's mass-enhancement parameter as follows

$$\gamma_S = \frac{\pi^2 D(0)}{3} (1 + \lambda). \quad (46)$$

The calculated γ_S agrees very well with the experimental value. For Re, Pt, and Pb, this agreement is improved by including SOI; Since these heavy elements have large SOI, this interaction is crucial to reproduce the experimental Sommerfeld coefficient.

We plot the computed- and experimental- T_c data contained in Fig. 2 into Fig. 4 to see the effect by SOI and SF. From this figure, we can see the following trends:

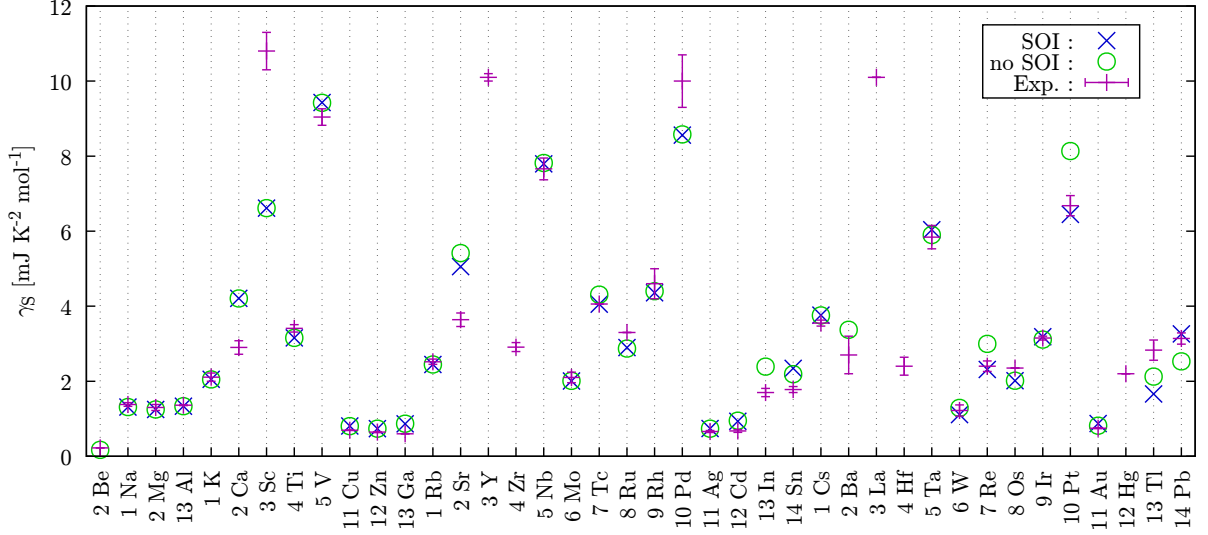


FIG. 3. Theoretical and experimental³⁵ Sommerfeld coefficient γ_S . The horizontal axis is the atomic symbol together with the group of the periodic table. Blue crosses and green circles indicate the Sommerfeld coefficient computed with and without SOI while magenta “+” with an error var indicates the experimental value of the Sommerfeld coefficient.

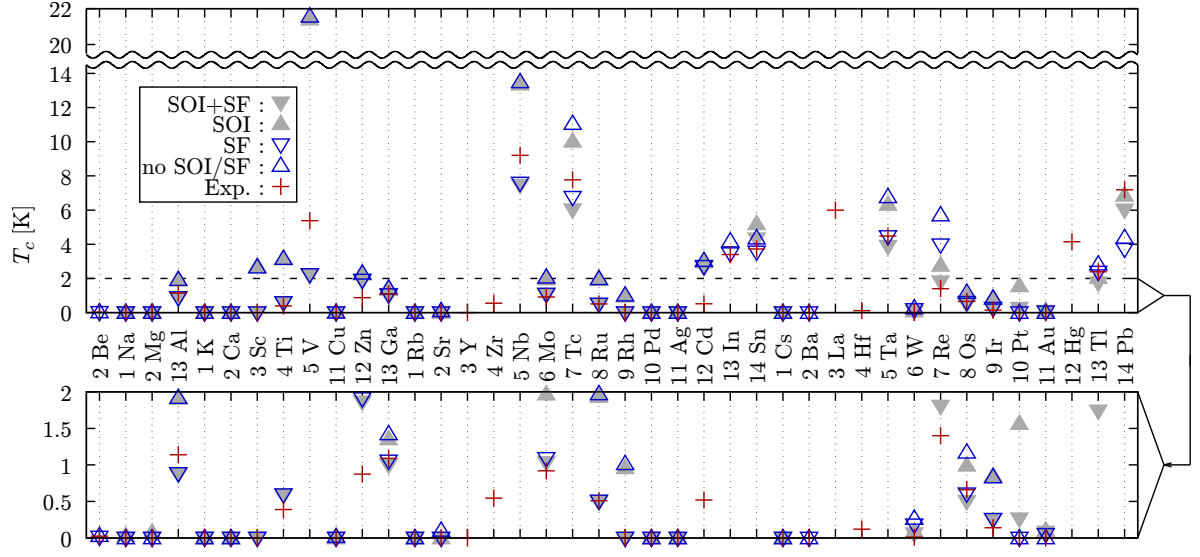


FIG. 4. Theoretical and experimental T_c s. The horizontal axis is the atomic symbol together with the group of the periodic table. Downward (upward) triangles indicate the T_c s computed with (without) SF. Filled (empty) triangles indicate the T_c s computed with (without) SOI. “+” indicates the experimental value of T_c . The plot which ranges from zero to two Kelvin in the upper panel is magnified into the bottom panel.

SF always reduces T_c s for these elemental systems. This reduction becomes significant for the transition metals and is crucial to reproduce the experimental T_c quantitatively. The mechanism of this reduction is detailed in the previous studies^{36,37}. In the transition metals, the effect of SF weakens with the increasing of the period in the periodic table. For example, μ_s varies 0.722 (V) \rightarrow 0.203 (Nb) \rightarrow 0.131 (Ta), 0.057 (Mo) \rightarrow 0.018 (W),

0.117 (Tc) \rightarrow 0.057 (Re), 0.122 (Ru) \rightarrow 0.055 (Os), and 0.269 (Rh) \rightarrow 0.108 (Ir). Also, the μ_s of Pd becomes negative; this indicates the formulation of SF breaks down due to the magnetic order. Although this magnetic order is a numerical artifact, this result shows that Pd has larger SF than that of Pt. This trend of SF is explained as follows³⁷: The electronic orbitals become delocalized with the increasing of the principal quantum number (3d

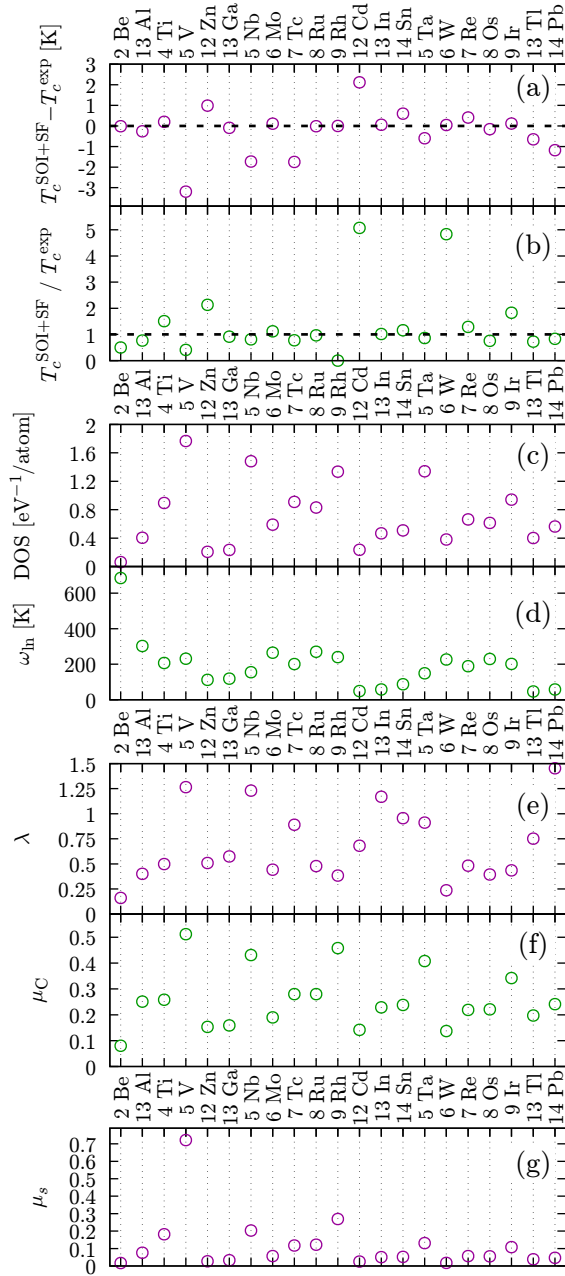


FIG. 5. We plot the following quantities for the elemental systems which have finite T_c : (a) The difference between the experimental T_c (T_c^{exp}) and theoretical T_c computed with SOI and SF ($T_c^{\text{SOI+SF}}$). (b) The ratio between T_c^{exp} and $T_c^{\text{SOI+SF}}$. (c) The density of states at the Fermi level. (d) The averaged phonon frequencies ω_{ln} . (e) The Fröhlich's mass-enhancement parameter λ . (f) The averaged Coulomb interaction μ_C in Eq. (42). (g) The averaged SF term μ_s in Eq. (43). The horizontal axis is the atomic symbol together with the group of the periodic table. We note that since there is no computed data for Be and In with SOI, we show the data for them without SOI.

→ 4d → 5d); this delocalization decreases the magnetic exchange-correlation kernel in Eq. (23). Also, the delo-

calized orbital has small DOS. Therefore, the elements in the larger period have smaller SF contribution. We cannot see this trend in the alkaline metals. For these elements, μ_s does not decrease with the increasing of the period, i.e., this parameter varies 0.213 (Na) → 0.270 (K) → 0.280 (Rb) → 0.427 (Cs). This behavior comes from the increasing of DOS because of the larger lattice constant (larger atomic radius) at the alkaline metals at the larger period. The effect of SOI is small in most cases, excepting Tc, Sn, Re, Tl, Pb. In these elements, the Fröhlich's parameter λ changes drastically by turning on the SOI. For Pb, this enhancement of λ (1.036 → 1.453) can be traced back to the three contributions i.e., the phonon softening (ω_{ln} decreases from 67 K to 58 K), the increased DOS at Fermi level (0.527 eV⁻¹ → 0.564 eV⁻¹), and the enhanced deformation potential $\delta^{97}V_{\text{KS}}(\mathbf{r})$ due to the SOI term¹⁹. These effects of SOI in Tc, Re, and Tl are opposite to ones in Pb and Sn; SOI reduces the electron-phonon coupling as well as T_c in these three materials. We can reproduce the absence of the superconductivity in alkaline, alkaline earth, and noble metals, excepting Pt and Au with SOI and SF; we observe small finite T_c for these two elements. We can reproduce the non-superconductivity also in Sc by including SF while we observe $T_c = 2.711$ K by ignoring SF. Since Sc has highly localized 3d electrons, the SF largely reduces T_c . For the group 12 elements (Zn and Cd), T_c s are overestimated even if we include SF. For these materials, the SF effect is small because the d orbitals are fully occupied.

Finally, we try to find the factor which dominates the accuracy of T_c . In Fig. 5, we plot the following quantities for the elemental systems which have finite T_c : (a) The difference between the experimental T_c (T_c^{exp}) and theoretical T_c computed with SOI and SF ($T_c^{\text{SOI+SF}}$). (b) The ratio between T_c^{exp} and $T_c^{\text{SOI+SF}}$. (c) The density of states at the Fermi level. (d) The averaged phonon frequencies ω_{ln} in Eq. (39). (e) The Fröhlich's mass-enhancement parameter λ in Eq. (38). (f) The averaged Coulomb interaction μ_C in Eq. (42). (g) The averaged SF term μ_s in Eq. (43). Note that since there is no computed data for Be and In with SOI, we show data for them without SOI. T_c s of Zn and Cd (V, Nb, Tc, Pb) are overestimated (underestimated) in the differential plot (a) while those of Zn Cd, W, Ir (Be, V, Rh) are overestimated (underestimated) in the ratio plot (b). Therefore, V, Zn, and Cd should be focused on to examine the accuracy of T_c , and we tried to find features of these two materials from elemental systems. From Fig. 5 (g), we can see that V has extremely large μ_s . When the system has large SF, the SF-mediated interaction in Eq. (31) changes rapidly because the inverse of the matrix in Eq. (44) approaches to a singular matrix. Therefore, we need to compute the SF of such systems more precisely, for example, by including the gradient collection into the magnetic exchange-correlation kernel in Eq. (23). On the other hand, it is difficult to see the significant difference between Zn, Cd, and other materi-

als. For example, these parameters of Ga are very close to those of Zn. However, the calculated T_c of Ga agrees with the experimental one very well.

Finally, by leaving from the superconductivity, we can see the following features from Fig. 5: DOS and μ_C show very similar behavior. Since μ_C in Eq. (42) can be approximated to the DOS times the averaged Coulomb interaction, this synchronicity indicates that these elemental materials have almost the same screened Coulomb repulsion. ω_{in} has peaks around group 6-9 on both periods 5 and 6. Also, the frequencies at both peaks are very close, although the atomic masses of these periods are different. These behaviors can be explained by the following Friedel's theory³⁸. The materials at group 6-9 have high cohesive energy because of the half-filled d-orbitals. This high cohesive energy leads the hardness and the high phonon frequencies of these materials. Since 5d orbitals are more delocalized than 4d orbitals, the binding energy increases for 5d materials. Therefore, the phonon frequency is unchanged because of the cancellation between the atomic mass and the stronger bonding.

VI. SUMMARY

In this study, we performed the benchmark calculations of SCDFE by using our open-source software package SUPERCONDUCTING TOOLKIT which uses our newly developed method for treating SOI together with SF. We showed benchmark results of superconducting properties calculated by SCDFE for 35 elemental materials together with computational details, and discussed the accuracy of the predicted T_c and the effects of SF and SOI up on T_c . We found that the calculations, including SOI and SF, reproduce quantitatively the experimental T_c s. The

SF is essential especially for the transition metals, and the effect of SOI is small for elemental systems excepting Tc, Sn, Re, Tl, and Pb. We also reproduced the absence of the superconductivity in the alkaline, alkaline earth, and noble metals. These result can be used to check the validity of further study such as the high-throughput calculation for exploring new superconductors. Moreover, the knowledge of this benchmark can be used to improve the methodology of SCDFE. For example, we can focus on Zn and Cd as a target for the next theoretical improvement. It is straightforward to extend the current benchmark calculation into the binary, ternary, and quaternary systems. From such a benchmark, we can check systematically the accuracy of SCDFE for the compound superconductors such as magnesium diboride³⁹, cuprates⁴⁰, iron-based⁴¹, and heavy-fermion superconductors⁴², etc. This kind of benchmark calculation should be done whenever there is room for theoretical improvements so that the applicability of SCDFE can be extended as a universal tool.

ACKNOWLEDGMENTS

We thank Ryosuke Akashi for the fruitful discussion about the spin-fluctuation. This work was supported by Priority Issue (creation of new functional devices and high-performance materials to support next-generation industries) to be tackled by using Post 'K' Computer from the MEXT of Japan. Y. H. is supported by Japan Society for the Promotion of Science through Program for Leading Graduate Schools (MERIT). The numerical calculations in this paper were done on the supercomputers in ISSP and Information Technology Center at the University of Tokyo.

* mkawamura@issp.u-tokyo.ac.jp

- ¹ L. N. Oliveira, E. K. U. Gross, and W. Kohn, *Phys. Rev. Lett.* **60**, 2430 (1988).
- ² M. Lüdgers, M. A. L. Marques, N. N. Lathiotakis, A. Floris, G. Profeta, L. Fast, A. Continenza, S. Massidda, and E. K. U. Gross, *Phys. Rev. B* **72**, 024545 (2005).
- ³ E. R. Margine and F. Giustino, *Phys. Rev. B* **87**, 024505 (2013).
- ⁴ W. L. McMillan, *Phys. Rev.* **167**, 331 (1968).
- ⁵ R. Dynes, *Solid State Commun.* **10**, 615 (1972).
- ⁶ A. Sanna, J. A. Flores-Livas, A. Davydov, G. Profeta, K. Dewhurst, S. Sharma, and E. K. U. Gross, *Journal of the Physical Society of Japan* **87**, 041012 (2018), <https://doi.org/10.7566/JPSJ.87.041012>.
- ⁷ F. Essenberg, A. Sanna, A. Linscheid, F. Tandezky, G. Profeta, P. Cudazzo, and E. K. U. Gross, *Phys. Rev. B* **90**, 214504 (2014).
- ⁸ M. A. L. Marques, M. Lüdgers, N. N. Lathiotakis, G. Profeta, A. Floris, L. Fast, A. Continenza, E. K. U. Gross, and S. Massidda, *Phys. Rev. B* **72**, 024546 (2005).

- ⁹ A. Floris, G. Profeta, N. N. Lathiotakis, M. Lüdgers, M. A. L. Marques, C. Franchini, E. K. U. Gross, A. Continenza, and S. Massidda, *Phys. Rev. Lett.* **94**, 037004 (2005).
- ¹⁰ A. Sanna, G. Profeta, A. Floris, A. Marini, E. K. U. Gross, and S. Massidda, *Phys. Rev. B* **75**, 020511 (2007).
- ¹¹ G. Profeta, C. Franchini, N. N. Lathiotakis, A. Floris, A. Sanna, M. A. L. Marques, M. Lüdgers, S. Massidda, E. K. U. Gross, and A. Continenza, *Phys. Rev. Lett.* **96**, 047003 (2006).
- ¹² P. Cudazzo, G. Profeta, A. Sanna, A. Floris, A. Continenza, S. Massidda, and E. K. U. Gross, *Phys. Rev. Lett.* **100**, 257001 (2008).
- ¹³ R. Akashi, M. Kawamura, S. Tsuneyuki, Y. Nomura, and R. Arita, *Phys. Rev. B* **91**, 224513 (2015).
- ¹⁴ F. Essenberg, A. Sanna, P. Buczek, A. Ernst, L. Sandratskii, and E. K. U. Gross, *Phys. Rev. B* **94**, 014503 (2016).
- ¹⁵ R. Akashi and R. Arita, *Phys. Rev. Lett.* **111**, 057006 (2013).

- ¹⁶ T. Nomoto, M. Kawamura, T. Koretsune, R. Arita, T. Machida, T. Hanaguri, M. Kriener, and Y. Taguchi, Submitted.
- ¹⁷ A. Seko, A. Togo, H. Hayashi, K. Tsuda, L. Chaput, and I. Tanaka, Phys. Rev. Lett. **115**, 205901 (2015).
- ¹⁸ A. Görling and M. Levy, Phys. Rev. A **50**, 196 (1994).
- ¹⁹ R. Heid, K.-P. Bohnen, I. Y. Sklyadneva, and E. V. Chulkov, Phys. Rev. B **81**, 174527 (2010).
- ²⁰ S. Baroni, S. de Gironcoli, A. Dal Corso, and P. Giannozzi, Rev. Mod. Phys. **73**, 515 (2001).
- ²¹ M. Gell-Mann and K. Brueckner, Phys. Rev. **106**, 364 (1957).
- ²² E. K. U. Gross and W. Kohn, Phys. Rev. Lett. **55**, 2850 (1985).
- ²³ M. Kawamura, R. Akashi, and S. Tsuneyuki, Phys. Rev. B **95**, 054506 (2017).
- ²⁴ E. Runge and E. K. U. Gross, Phys. Rev. Lett. **52**, 997 (1984).
- ²⁵ J. Bardeen, L. N. Cooper, and J. R. Schrieffer, Phys. Rev. **108**, 1175 (1957).
- ²⁶ J. Schrieffer, *Theory of Superconductivity*, Advanced Book Program Series (Advanced Book Program, Perseus Books, (1983)).
- ²⁷ P. Giannozzi, O. Andreussi, T. Brumme, O. Bunau, M. B. Nardelli, M. Calandra, R. Car, C. Cavazzoni, D. Ceresoli, M. Cococcioni, N. Colonna, I. Carnimeo, A. D. Corso, S. de Gironcoli, P. Delugas, R. A. D. Jr, A. Ferretti, A. Floris, G. Fratesi, G. Fugallo, R. Gebauer, U. Gerstmann, F. Giustino, T. Gorni, J. Jia, M. Kawamura, H.-Y. Ko, A. Kokalj, E. Küçükbenli, M. Lazzeri, M. Marsili, N. Marzari, F. Mauri, N. L. Nguyen, H.-V. Nguyen, A. O. de-la Roza, L. Paulatto, S. Poncé, D. Rocca, R. Sabatini, B. Santra, M. Schlipf, A. P. Seitsonen, A. Smogunov, I. Timrov, T. Thonhauser, P. Umari, N. Vast, X. Wu, and S. Baroni, Journal of Physics: Condensed Matter **29**, 465901 (2017).
- ²⁸ J. P. Perdew, K. Burke, and M. Ernzerhof, Phys. Rev. Lett. **78**, 1396 (1997).
- ²⁹ D. R. Hamann, Phys. Rev. B **88**, 085117 (2013).
- ³⁰ M. Schlipf and F. Gygi, Computer Physics Communications **196**, 36 (2015).
- ³¹ G. Prandini, A. Marrazzo, I. E. Castelli, N. Mounet, and N. Marzari, npj Computational Materials **4**, 72 (2018).
- ³² M. Kawamura, Y. Gohda, and S. Tsuneyuki, Phys. Rev. B **89**, 094515 (2014).
- ³³ <http://sctk.osdn.jp/>.
- ³⁴ J. Hamlin, Physica C: Superconductivity and its Applications **514**, 59 (2015), superconducting Materials: Conventional, Unconventional and Undetermined.
- ³⁵ K. A. Gschneidner, in *Solid State Physics: Advances in Research and Applications*, Vol. 16, edited by F. Seitz and D. Turnbull (Academic Press, 1964) p. 275.
- ³⁶ N. F. Berk and J. R. Schrieffer, Phys. Rev. Lett. **17**, 433 (1966).
- ³⁷ K. Tsutsumi, Y. Hizume, M. Kawamura, R. Akashi, and S. Tsuneyuki, To be submitted.
- ³⁸ J. Friedel, in *Theory of Magnetism in Transition Metals*, edited by Marshall, W. (Academic Press, 1967) p. 283.
- ³⁹ J. Nagamatsu, N. Nakagawa, T. Muranaka, Y. Zenitani, and J. Akimitsu, Nature (London) **410**, 63 (2001).
- ⁴⁰ N. Plakida, in *High-Temperature Cuprate Superconductors: Experiment, Theory, and Applications*, Springer Series in Solid-State Sciences, Vol. 166 (2010) pp. 1–570.
- ⁴¹ G. R. Stewart, Rev. Mod. Phys. **83**, 1589 (2011).
- ⁴² C. Pfleiderer, Rev. Mod. Phys. **81**, 1551 (2009).